

Electron delocalization enhances the thermoelectric performance of misfit layer compound $(Sn_{1-x}Bi_xS)_{1.2}(TiS_2)_2$

Xin Zhao(赵昕), Xuanwei Zhao(赵轩为), Liwei Lin(林黎蔚), Ding Ren(任丁), Bo Liu(刘波), and Ran Ang(昂然)
Citation: Chin. Phys. B, 2022, 31 (**11**): 117202. DOI: 10.1088/1674-1056/ac6493

What follows is a list of articles you may be interested in

Group velocity matters for accurate prediction of phonon-limited carrier mobility

Qiao-Lin Yang(杨巧林), Hui-Xiong Deng(邓惠雄), Su-Huai Wei(魏苏淮), and Jun-Wei Luo(骆军委)
Chin. Phys. B, 2021, 30 (**8**): 087201. DOI: 10.1088/1674-1056/ac0133

Effect of Nb doping on microstructures and thermoelectric properties of $SrTiO_3$ ceramics

Da-Quan Liu(刘达权), Yu-Wei Zhang(张玉伟), Hui-Jun Kang(康慧君), Jin-Ling Li(李金玲), Xiong Yang(杨雄), Tong-Min Wang(王同敏)
Chin. Phys. B, 2018, 27 (**4**): 047205. DOI: 10.1088/1674-1056/27/4/047205

First-principles hybrid functional study of the electronic structure and charge carrier mobility in perovskite $CH_3NH_3SnI_3$

Li-Juan Wu(伍丽娟), Yu-Qing Zhao(赵宇清), Chang-Wen Chen(陈畅文), Ling-Zhi Wang(王琳芝), Biao Liu(刘标), Meng-Qiu Cai(蔡孟秋)
Chin. Phys. B, 2016, 25 (**10**): 107202. DOI: 10.1088/1674-1056/25/10/107202

High temperature characteristics of bilayer epitaxial graphene field-effect transistors on SiC Substrate

Ze-Zhao He(何泽召), Ke-Wu Yang(杨克武), Cui Yu(蔚翠), Qing-Bin Liu(刘庆彬), Jing-Jing Wang(王晶晶), Jia Li(李佳), Wei-Li Lu(芦伟立), Zhi-Hong Feng(冯志红), Shu-Jun Cai(蔡树军)
Chin. Phys. B, 2016, 25 (**6**): 067206. DOI: 10.1088/1674-1056/25/6/067206

Radio-frequency transistors from millimeter-scale graphene domains

Wei Zi-Jun (魏子钧), Fu Yun-Yi (傅云义), Liu Jing-Bo (刘竞博), Wang Zi-Dong (王紫东), Jia Yue-Hui (贾越辉), Guo Jian (郭剑), Ren Li-Ming (任黎明), Chen Yuan-Fu (陈远富), Zhang Han (张酣), Huang Ru (黄如), Zhang Xing (张兴)
Chin. Phys. B, 2014, 23 (**11**): 117201. DOI: 10.1088/1674-1056/23/11/117201

SPECIAL TOPIC — Progress in thermoelectric materials and devices

Electron delocalization enhances the thermoelectric performance of misfit layer compound $(Sn_{1-x}Bi_xS)_{1.2}(TiS_2)_2$

Xin Zhao(赵昕)[1,†], Xuanwei Zhao(赵轩为)[1,†], Liwei Lin(林黎蔚)[1,‡], Ding Ren(任丁)[1], Bo Liu(刘波)[1], and Ran Ang(昂然)[1,2,§]

[1] *Key Laboratory of Radiation Physics and Technology, Ministry of Education, Institute of Nuclear Science and Technology, Sichuan University, Chengdu* 610064, *China*

[2] *Institute of New Energy and Low-Carbon Technology, Sichuan University, Chengdu* 610065, *China*

(Received 17 March 2022; revised manuscript received 1 April 2022; accepted manuscript online 6 April 2022)

The misfit layer compound $(SnS)_{1.2}(TiS_2)_2$ is a promising low-cost thermoelectric material because of its low thermal conductivity derived from the superlattice-like structure. However, the strong covalent bonds within each constituent layer highly localize the electrons thereby it is highly challenging to optimize the power factor by doping or alloying. Here, we show that Bi doping at the Sn site markedly breaks the covalent bonds networks and highly delocalizes the electrons. This results in a high charge carrier concentration and enhanced power factor throughout the whole temperature range. It is highly remarkable that Bi doping also significantly reduces the thermal conductivity by suppressing the heat conduction carried by phonons, indicating that it independently modulates phonon and charge transport properties. These effects collectively give rise to a maximum ZT of 0.3 at 720 K. In addition, we apply the single Kane band model and the Debye–Callaway model to clarify the electron and phonon transport mechanisms in the misfit layer compound $(SnS)_{1.2}(TiS_2)_2$.

Keywords: misfit layer sulfide, electron delocalization, carrier mobility, chemical bond

PACS: 72.15.Jf, 73.61.Ga, 73.90.+f, 74.25.F– **DOI:** 10.1088/1674-1056/ac6493

1. Introduction

Over 60% fossil fuels input for power generation is being rejected as low-grade heat annually.[1] Thermoelectric materials are able to directly convert such a huge amount of heat into utilizable electricity[2] without releasing any chemical residuals, showing great potential to contribute to solving the energy problem at present.[3,4] The efficiency of a thermoelectric device primary depends on the figure of merit, namely, ZT, of the thermoelectric materials used, which is defined as $ZT = S^2\sigma T/\kappa_{tot}$,[4] where S represents Seebeck coefficient, σ denotes electrical conductivity, their product $S^2\sigma$ is called power factor, T is the absolute temperature, and κ_{tot} is the total thermal conductivity with contribution from both charge carriers (κ_{ele}) and phonons (κ_{lat}).

In the past decades, the ZT values of representative thermoelectric compounds have been considerably improved by applying innovative strategies, such as optimizing electrical transport properties[5–10] or suppressing κ_{lat}.[11,12] However, the majority thermoelectric materials contain toxic or expensive elements. For extensive application, thermoelectric community currently puts interest on searching economically-viable, environmentally benign thermoelectric materials.[13–15] The surprising and promising examples are the discovery of Mg_3Sb_2[8,16–18] and SnSe[19–22] based compounds with intrinsically low thermal conductivity. The former shows exceptionally high ZT value of ~ 1.5 around room temperature, exceeded conventional expensive Bi_2Te_3.[8,16,17] The latter exhibits extraordinary performance over a broad temperature window. Besides, the study of the physical mechanisms of novel materials is also very important. The single crystal 1T-TaS_2 sample exhibits strong coupling between phonon excitation and commensurate charge-density-wave lattice, which provides a deep insight into close association between electronic correlation and dynamical motions of phonons.[23] These findings unambiguously highlight the importance of discovering new compounds.

$(SnS)_{1.2}(TiS_2)_2$ is an n-type misfit layer semiconductor built by alternately stacking two atomically thin TiS_2 slabs with a van der Waals (vdW) gap and SnS monolayer along the c crystallographic direction. Given the abundant interface formed between the TiS_2 and SnS layer, it shows intrinsically low thermal conductivity compared with other thermoelectric sulfides.[24,25] However, it is highly challenging to optimize its power factor because the metal cation easily forms covalent bonds with sulfur, highly localizing the electrons. For example, $(Sn_{0.96}Sb_{0.04}S)_{1.2}(TiS_2)_2$ shows carrier concentration nearly the same to the pristine one.[26] Here, we reveal that Bi doping can effectively improve the carrier concentration without degrading the carrier mobility by delocalizing the

†These authors contributed equally.

‡Corresponding author. E-mail: linliwei@scu.edu.cn

§Corresponding author. E-mail: rang@scu.edu.cn

© 2022 Chinese Physical Society and IOP Publishing Ltd

surrounding electrons. This gives rise to an enhanced power factor over the entire temperature investigated. Remarkably, the heavy Bi atom also significantly decreases the lattice thermal conductivity by generating point defects.[27] As a result, $(Sn_{0.96}Bi_{0.04}S)_{1.2}(TiS_2)_2$ shows a ZT value of 0.3 at 723 K, one of the highest values reported in this compound.

2. Experimental details

2.1. Synthesis and sample preparation

The appropriate molar ratio of high purity elements of tin (99.99%, aladdin), titanium (99.99%, aladdin), sulfur (99.99%, aladdin) and bismuth (99.999%, aladdin) corresponding to $(Sn_{1-x}Bi_xS)_{1.2}(TiS_2)_2$ ($x = 0, 0.02, 0.04, 0.06$) was sealed in a quartz tube under a high vacuum ($\sim 10^{-4}$ Pa). To minimize the risk of explosion, the sealed tubes were slowly heated to 773 K and dwelled for 12 h, afterward the temperature was raised to 1073 K and allowed to react for 48 h, and naturally cooled down to ambient temperature. The obtained ingots were hand-ground into fine powders in air using an agate and pestle. The resulting fine powder was loaded into a graphite die mold and hot pressed at 923 K for 45 min under an axial pressure of 50 MPa in a dynamic vacuum. The density of the sample was determined by the geometrical dimensions and masses, showing all the samples have density higher than 97.3% of the theoretical value.

2.2. Powder x-ray diffraction

The pulverized samples were used for powder x-ray diffraction (XRD). The powder diffraction patterns were recorded with Cu $K\alpha$ ($\lambda = 1.5418$ Å) radiation in a reflection geometry on an Inel diffractometer operating at 40 kV and 20 mA (DX-2700 x-ray diffractometer). All measured samples are single phase within the detection limit of our laboratory XRD instrument, showing none of detectable secondary phases and unreacted elements.

2.3. Charge carrier transport

The densified samples were cut into different shapes using a wire saw for charge and thermal transport properties measurement respectively. The rectangular bar with the dimension of $2 \times 3 \times 8$ mm^3 was used for simultaneously measuring the electrical conductivity and Seebeck coefficient employing a CTApro instrument under a low-pressure helium atmosphere from 320 K to 720 K. The Hall charge carrier concentration and mobility were measured from 320 K to 720 K by a home-built apparatus with a unidirectional 1.5 T magnetic field under a high vacuum.

2.4. Thermal conductivity

Thermal diffusivities with respect to temperature were measured using disks with a diameter of 6 mm or 8 mm and a thickness of 1.5 mm using the laser flash diffusivity method on a Netzsch LFA 467 instrument. The surface of the disks was protected by a thin layer of graphite to minimize the thermal radiation at elevate temperature. The thermal conductivity was calculated by the equation $\kappa_{tot} = \rho \cdot D \cdot C_p$, where ρ is the mass density, D is the measured thermal diffusivity, and C_p represents the temperature-dependent heat capacity that can be determined by $C_p = [0.17078 + (2.64876 \times 10^{-5}) \times T]$ J·g^{-1}·K^{-1}, where T is the absolute temperature. The electrical contribution to the total thermal conductivity was calculated based on the relation $\kappa_{ele} = L\sigma T$, where L is the Lorenz number estimated using a single parabolic band (see supporting information for the details), σ is the electrical conductivity, and T is the absolute temperature. Lattice thermal conductivity κ_{lat} was calculated by the relation $\kappa_{lat} = \kappa_{tot} - \kappa_{ele}$.

2.5. Electronic structure calculation

The first-principles calculations were performed by utilizing the Perdew–Burke–Ernzerhof (PBE)[28] formalism and generalized gradient approximation (GGA)[29,30] implemented in Vienna *ab initio* simulation package (VASP)[31,32] code. The plane-wave basis was truncated at the energy cutoff of 600 eV. To reduce the computational load, we only sampled the momentum space at the Γ-point and a $4 \times 1 \times 1$ mesh. All geometry structures were fully relaxed until the calculated Hellmann–Feynman force on every atom were less than 0.03 eV·Å^{-1} under the convergence condition of 10^{-4} eV.

3. Results and discussion

Covalent bonds in $(SnS)_{1.2}(TiS_2)_2$ strongly trap the electrons so that softening these bonds may release the localized electrons. Note that, the bond dissociation energy for Bi–S is 315 kJ·mol^{-1}, much lower than 467 kJ·mol^{-1} for Sn–S and 387 kJ·mol^{-1} for Sb–S.[33] This indicates Bi doping can weaken the covalent bonds and give rise to a higher carrier concentration than the Sb doped system. To verify our hypothesis, we synthesized samples with the composition of $(Sn_{1-x}Bi_xS)_{1.2}(TiS_2)_2$ ($x = 0, 0.02, 0.04, 0.06$) using high-temperature solid-state reaction. All the phases can be fully indexed as the misfit layer structure, showing neither detectable impurity phases nor unreacted residual within the resolution limit of lab XRD measurements (Fig. 1(a) and Fig. S1). To accurately determine the lattice parameter, we performed Rietveld refinement on the recorded XRD patterns (Fig. S2 and Table S1). The refined unit cell dimensions gradually shrink as the Bi content increases, suggesting that Bi atoms are homogenously dissolved over the matrix apparently (Fig. 1(b)). This finding agrees well with the microscopic elemental map collected by scanning electron microscopy equipped with an energy dispersive spectroscopy (SEM-EDS, Fig. S3).

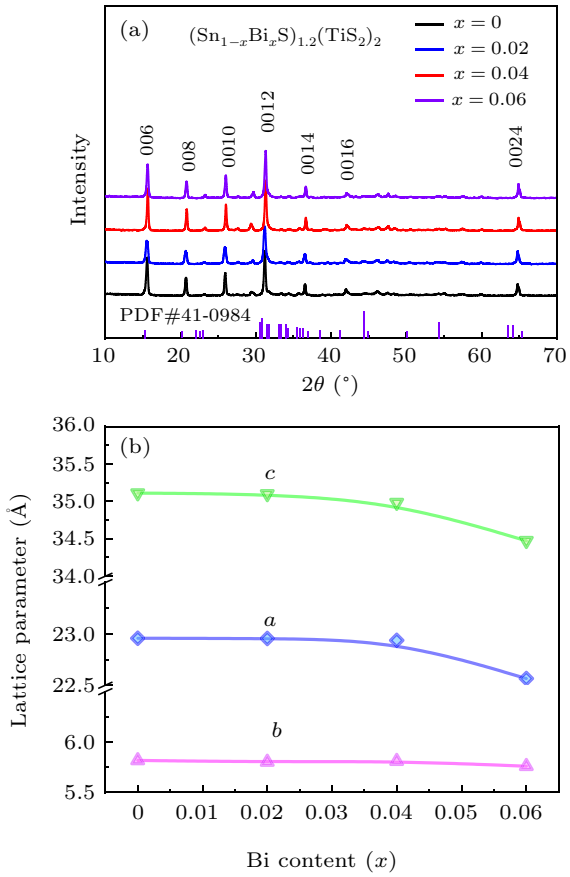


Fig. 1. (a) Powder XRD patterns of $(Sn_{1-x}Bi_xS)_{1.2}(TiS_2)$ samples ($x = 0, 0.02, 0.04, 0.06$). (b) Lattice parameters with respect to the Bi content.

Trivalent Bi^{3+} substituting divalent Sn^{2+} could increase charge carrier properties significantly. In accordance, we measured the temperature-dependent Hall carrier concentration and mobility for the $(Sn_{1-x}Bi_xS)_{1.2}(TiS_2)_2$ ($x = 0, 0.02, 0.04, 0.06$) samples. Note that although we measured all properties along both parallel and perpendicular to the hot press direction, we will mainly concentrate on those perpendicular to the press direction because it shows higher ZT. The transport properties collected parallel to the press direction are shown in Fig. S4. As the concentration of Bi doping increases, we can see an enhancement of the electrical properties. This is consistent with the results observed in the in-plane, which also can confirm our hypothesis.

All samples show nearly constant Hall carrier concentration (n_H) over the entire temperature range investigated, and their values monotonously increase with higher Bi concentration (Fig. 2(a)). It should be noted that the electron doping efficiency, namely, the number of electrons per Bi atom to the matrix is markedly higher than previously reported values for other dopants in $(SnS)_{1.2}(TiS_2)$-based materials. For example, $x = 0.04$ sample shows n_H of 1.8×10^{21} cm^{-3} at 300 K, indicating its electron doping efficiency amounts to 0.63 e$^-$. In sharp contrast, $(Sn_{0.96}Sb_{0.04}S)_{1.2}(TiS_2)$ exhibits an n_H close to the matrix at 300 K as indicated by the green dashed line,[26] revealing Sb has negligible electron doping efficiency. These verify that Bi atom acts as an efficient electron donor to the $(SnS)_{1.2}(TiS_2)$ lattice.

Although Bi doping considerably increases the n_H, it marginally reduces the charge carrier mobility (μ_H). In fact, all samples exhibit nearly identical μ_H over the entire temperature range (Fig. 2(b)). Their values rapidly drop with the raising temperature, following the same power law trend of $\sim T^{-1.5}$ over the entire temperature range, which evident the phonon scattering dominates the charge carrier scattering.

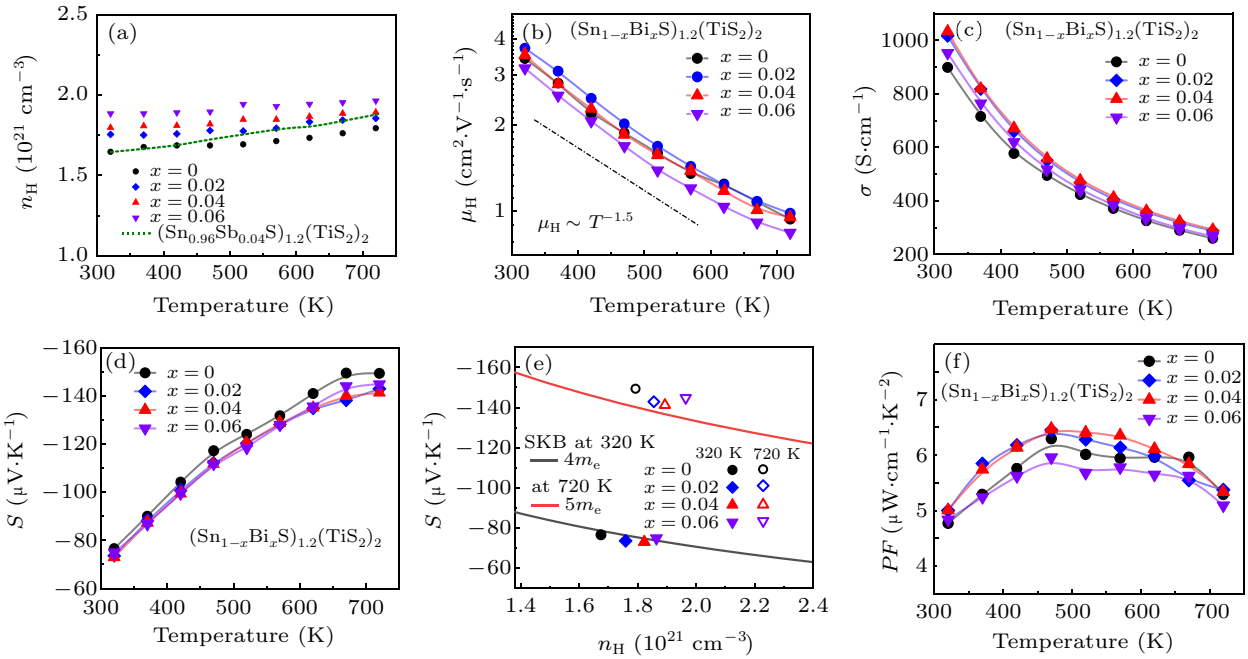


Fig. 2. Charge transport properties of the $(Sn_{1-x}Bi_xS)_{1.2}(TiS_2)_2$ samples ($x = 0, 0.02, 0.04, 0.06$). (a) Temperature-dependent Hall carrier concentration n_H. The experimental data of $(Sn_{0.96}Sb_{0.04}S)_{1.2}(TiS_2)_2$ from previously report is included for comparison (green dashed line).[26] (b) Temperature dependent Hall mobility μ_H, (c) conductivity σ and (d) Seebeck coefficient. (e) Carrier concentration-dependent Seebeck coefficient at 320 K and 720 K. (f) Temperature-dependent power factor.

This observation confirms Bi uniformly spreading over the crystalline matrix, rather than forming secondary phases or aggregate at the grain boundary, otherwise the μ_H would be significantly decreased. Indeed, it contrasts with the general understanding that increasing charge carrier concentration usually decreases with raising n_H because of enhanced carrier–carrier scattering, implying Bi doping marginally affects the charge carrier transport.

Figure 2(c) shows the electrical conductivity (σ) with respect to temperature for the $(Sn_{1-x}Bi_xS)_{1.2}(TiS_2)_2$ ($x = 0, 0.02, 0.04, 0.06$) samples. Because Bi doping markedly improves the n_H with negligible degrading μ_H in the full temperature range, it gives rise to higher σ at every single temperature point compared to the pristine sample. For example, the σ of the title compound $(Sn_{0.96}Bi_{0.04}S)_{1.2}(TiS_2)$ is ~ 1100 S·cm^{-1} and ~ 300 S·cm^{-1} at 300 K and 723 K, respectively, much higher than ~ 900 S·cm^{-1} and 250 S·cm^{-1} at the same temperature for the pristine sample.

The Seebeck coefficient (S) of all samples is negative over the entire temperature range, demonstrating they are n-type semiconductor (Fig. 2(d)). Note that Bi doping marginally impacts the magnitude of Seebeck among samples because all the samples have very high n_H on the order of $\sim 10^{21}$ cm^{-3}. To examine any possible modulation in electron effective mass m^*, we calculated the theoretical Pisarenko relation between S and n_H for undoped $(SnS)_{1.2}(TiS_2)$ in the frame of single Kane band model by assuming that the phonon scattering governs the charge carrier scattering. The black and red lines denote $m^* = 4m_e$ at 320 K and $m^* = 5m_e$ at 720 K, respectively (Fig. 2(e)). The S values for all the samples in this work match well on the lines, suggesting that doped Bi does not alter the band structure in the vicinity of the Fermi level.

Due to the doped Bi considerably increases σ without significantly reducing S, it optimizes the power factor particularly for the best composition $(Sn_{0.96}Bi_{0.04}S)_{1.2}(TiS_2)$ (Fig. 2(f)). In fact, the $(Sn_{0.96}Bi_{0.04}S)_{1.2}(TiS_2)$ sample shows a power factor higher than the pristine one over the entire temperature range. Note that it is challenging to improve the power factor of misfit layer compounds because the highly distorted interface derived from the constituent layers typically leads to a very low electrical conductivity and thereby a low power factor.

To better understand the enhanced charge transport properties in the $(Sn_{1-x}Bi_xS)_{1.2}(TiS_2)_2$ compounds, we carried out first-principles calculation within density functional theory regime. Given the high electron doping efficiency as we discussed earlier, the doped Bi atom was placed at the Sn site to mimic the experimental observation. We first analyzed the charge transfer in Bi doped $(SnS)_{1.2}(TiS_2)$ for examining the possible charge transfer between Bi and the matrix. For clarity, we only display the charge transfer between one TiS_2 layer and its neighboring SnS slab (Fig. 3(a)). The result shows that the electrons of Bi flow toward the nearest sulfur atom in the adjunct TiS_2 layer as indicated by the blue ellipsoid, forming electronic bridge to connect large van der Waals gap and facilitate the charge transfer over the matrix. For comparison, we also similarly calculated the Sb doped $(SnS)_{1.2}(TiS_2)$. It reveals that the electrons from Sb atom are isolated between the van der Waals gap.

It is worth noting that quantitative Bader charge transfer analysis shows that Bi donates 1.27 e$^-$ to the interacting S atom, coincidentally to the value of 1.28 e$^-$ of Sb transferred to the system. This supports our hypothesis that Bi doping weakly localized the electrons. We calculated the electron localization function (ELF) for both Bi and Sb doped systems (Figs. 3(c) and 3(d)). This measures the electron localization

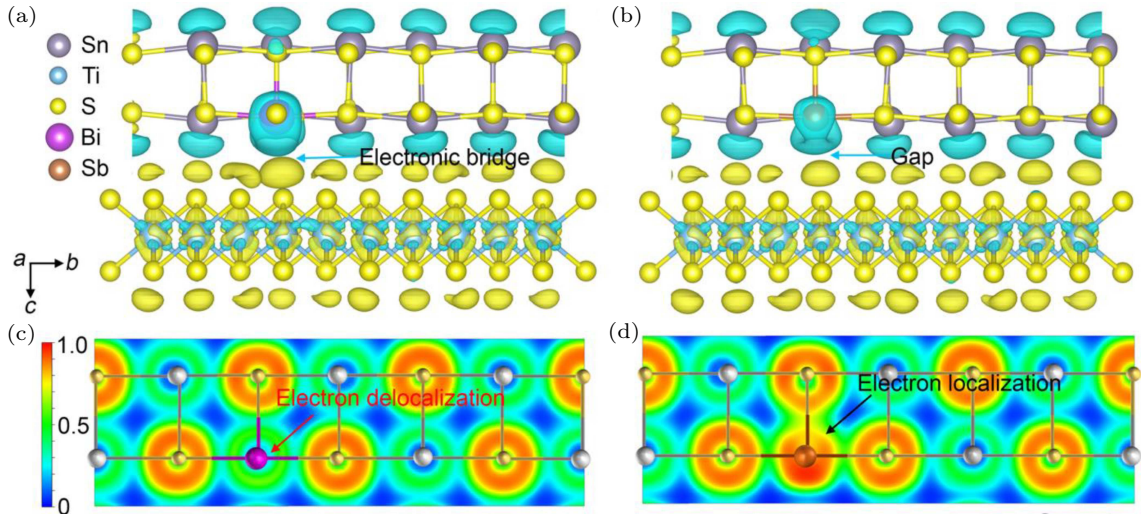


Fig. 3. The charge transfer analysis for (a) Bi and (b) Sb doped $(SnS)_{1.2}(TiS_2)$. The Sn, Ti, S, Bi and Sb atoms are depicted by grey, blue, yellow, violet, and orange spheres, respectively. Blue ellipsoids surrounding the atoms denote a loss of electrons. Electron localization function (ELF) contour mapped along the ⟨100⟩ zone axis for (a) Bi and (b) Sb doped $(SnS)_{1.2}(TiS_2)$. ELF values ranging from 0 to 1 are depicted by the color bar shown in (c), where blue color denotes the electrons with almost no localization or no electrons, and the red color corresponds to the perfect localization of electrons. The red arrow in (c) indicates Bi substituting Sn delocalized electrons. The black arrow in (d) points out the Sb atom forms covalent bond with adjunct sulfur atom, which heavily localized the electrons.

in atomic and molecular systems, directly evaluating the chemical interaction between the adjunct atoms.[34] The magnitude of ELF increases from 0 to 1 which denotes the electron transiting from no localization to perfect localization and is visualized by the color code varying from blue to red color. The ELF contour mapped along the ⟨100⟩ zone axis of Bi doped system reveals the ELF value between Bi and S atoms smaller than 0.5 (Fig. 3(c)). This indicates that electrons surrounding Bi are highly mobile, consistent with our observation that incorporating Bi atom negligibly affects μ_H. By contrast, electron localization domains are clearly observed between Sb and S atoms in Sb doped $(SnS)_{1.2}(TiS_2)$ as indicated by the black arrow. This suggests that the Sb atom is prone to form covalent bond with nearby sulfur atom, trapping the free electrons and reducing the electron doping efficiency. In fact, the EFL results agree well with the fact that the Bi–S bond has lower enthalpy and dissociation energy than the Sb–S bond as we discussed in the previously section, confirming that the weak bond contributes to the exceptionally charge transfer of Bi.

Figure 4(a) presents temperature-dependent total thermal conductivity (κ_{tot}) for the $(Sn_{1-x}Bi_xS)_{1.2}(TiS_2)_2$ samples ($x = 0, 0.02, 0.04, 0.06$). It is highly remarkable that all Bi-doped samples show suppressed κ_{tot} compared with the pristine sample despite they exhibit much higher σ than the latter. This observation implies that the Bi doping significantly impedes heat conduction by phonons. As a result, we extracted the lattice thermal conductivity κ_{lat} by invoking the Widemann–Franz law to subtract electronic thermal conductivity κ_{ele} from κ_{tot} (see Appendix A for details). All doped samples show much lower κ_{lat} than the undoped one (Fig. 4(b)). For example, the κ_{lat} at 320 K markedly decreases from ~ 1.7 W·m^{-1}·K^{-1} for the $x = 0$ sample to ~ 1.2 W·m^{-1}·K^{-1} for the $x = 0.04$ sample. To better understand the effect of Bi doping on thermal conductivity, we calculated the temperature-dependent κ_{lat} by the Debye–Callaway model. The black line represents the calculated κ_{lat} for the pristine sample (Fig. 4(b)), which only considers Umklapp (U) and normal (N) processes. The calculated results fit well with the experimental value, reflecting that the U and N processes dominate the phonon scattering. Since neither secondary phase nor element aggregation is present in the Bi doped samples, we further introduced point defects to the Bi doped system as indicated by the red dash line. The calculated value for the $x = 0.04$ sample lies far below the pristine one, supporting that the point defect contributes significantly to reducing κ_{lat}. In fact, the title compound $(Sn_{0.96}Bi_{0.04}S)_{1.2}(TiS_2)_2$ shows much lower κ_{lat} than that of previously reported thermoelectric sulfides (Fig. 4(c)). Similarly, the out-of-plane κ_{tot} is reached 0.7 W·m^{-1}·K^{-1} for the $x = 0.04$ sample at 723 K, as shown in Fig. S4(e). It should be noted that these data are close to our previous work about $(Sn_{1-x}Sb_xS)_{1.2}(TiS_2)_2$ and reflect the good reproducibility of the series of works.[26]

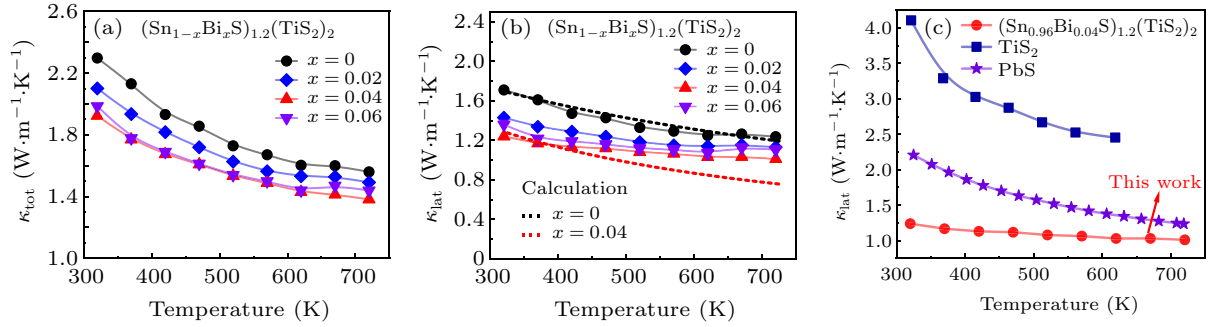


Fig. 4. Temperature-dependent (a) total thermal conductivity κ_{tot} and (b) lattice thermal conductivity κ_{lat} for $(Sn_{1-x}Bi_xS)_{1.2}(TiS_2)_2$ ($x = 0, 0.02, 0.04, 0.06$). The black and red dashed lines correspond to the calculated temperature-dependent κ_{lat} for the pristine and $x = 0.04$ samples using the Debye–Callaway model. (c) A κ_{lat} comparison with typical thermoelectric sulfides including TiS_2[25] and PbS.[24]

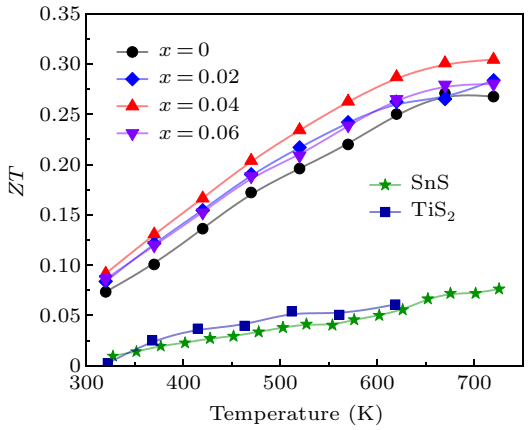


Fig. 5. Temperature-dependent ZT of $(Sn_{1-x}Bi_xS)_{1.2}(TiS_2)_2$ ($x = 0, 0.02, 0.04, 0.06$) samples. The ZT values of pristine TiS_2[25] and SnS[35] are given for comparison.

Figure 5 shows the temperature-dependent dimensionless figure of merit, ZT, for the $(Sn_{1-x}Bi_xS)_{1.2}(TiS_2)_2$ samples ($x = 0, 0.02, 0.04, 0.06$). The $(Sn_{0.96}Bi_{0.04}S)_{1.2}(TiS_2)_2$ exhibits higher ZT values over the entire temperature range with a maximum reaching to 0.3 at 720 K. It is one of the highest among misfit layer compounds. The achieved performance out-performs previously reported TiS_2 and state-of-the-art polycrystalline SnS, indicating its great potential as a low-cost thermoelectric material for power generation.

4. Conclusions

Misfit layer compounds emerge as promising low-cost thermoelectric sulfides. However, it is challenging to opti-

mize its carrier concentration because dopants tend to form covalent bond with sulfur. We demonstrated that Bi weakly bonded with sulfur, delocalized the charge carrier and facilitated the charge transfer. Highly mobile electrons significantly enhanced electrical conductivity and power factor of $(Sn_{0.96}Bi_{0.04}S)_{1.2}(TiS_2)_2$ over the entire temperature range. The heavy Bi atom also exceptionally reduced κ_{lat} by introducing mass fluctuation. By virtue of the Bi doping on charge and thermal transport properties, $(Sn_{0.96}Bi_{0.04}S)_{1.2}(TiS_2)_2$ shows a maximum ZT of 0.3 at 720 K, excelling many state-of-the-art thermoelectric sulfides including SnS and PbS.

Appendix A

Density of state mass calculation

The density of state mass (m^*) is calculated according to the following equations[36,37] using the Seebeck coefficient (S) and carrier concentration (n_H):

$$S = \frac{k_B}{e}\left[\left(\frac{(2+\lambda)F_{1+\lambda}(\mu)}{(1+\lambda)F_\lambda(\mu)}\right)^2 - \mu\right], \tag{A1}$$

$$F_j(\mu) = \int_0^\infty \frac{\zeta^j \mathrm{d}\zeta}{1+\mathrm{e}^{(\zeta-\mu)}}, \tag{A2}$$

$$m^* = \frac{h^2}{2k_BT}\left[\frac{n_H}{4\pi F_{1/2}(\mu)}\right]^{2/3}, \tag{A3}$$

where μ is the reduced Fermi level, $F_j(\mu)$ is the Fermi integral, k_B is the Boltzmann constant, h is the Planck constant, and $\lambda = 0$ is the scattering parameter corresponding to acoustic phonon scattering.

Lorenz number calculation

The Lorenz number L was obtained by single parabolic band (SPB) model with acoustic scattering ($\lambda = 0$ for acoustic phonon scattering):

$$L = \frac{k_B^2}{e^2}\left[\frac{\lambda+3}{\lambda+1}\cdot\frac{F_{\lambda+2}(\eta)}{F_\lambda(\eta)} - \left(\frac{\lambda+2}{\lambda+1}\right)^2\cdot\frac{F_{\lambda+1}^2(\eta)}{F_\lambda^2(\eta)}\right]. \tag{A4}$$

Debye–Callaway model simulation

The Debye–Callaway model has been utilized to calculate the lattice thermal conductivity involving the point defects induced phonon scattering.[38–40] The lattice thermal conductivity is calculated by using the following equations:[41,42]

$$U^2 = \left(\frac{\pi^2\theta_D\Omega}{h\nu^2}\right)\kappa_L^{pure}\Gamma, \tag{A5}$$

$$\kappa_L^{calc} = U^{-1}\tan^{-1}U\,\kappa_L^{pure}, \tag{A6}$$

where Ω, h, ν, θ_D, κ_L^{pure}, κ_L^{calc} and Γ_{calc} are the average volume/atom, the Planck constant, the average sound velocity, the Debye temperature, the lattice thermal conductivity of the pure materials, the calculated lattice thermal conductivity of defected materials and the disorder scattering parameter, respectively.

The disorder scattering parameter Γ_{calc} is calculated by the model of Slack[43] and by Abeles[42] assuming $\Gamma_{calc} = \Gamma_M + \Gamma_S$, where Γ_M and Γ_S are mass fluctuations scattering parameter and strain field fluctuations scattering parameter, respectively. The mass and strain fluctuation scattering parameters are determined by[40]

$$\Gamma_M = \frac{\sum_{k=1}^{n} c_k\left(\frac{\bar{M}_k}{\bar{\bar{M}}}\right)^2 f_k^1 f_k^2\left(\frac{M_k^1 - M_k^2}{\bar{M}_k}\right)^2}{\left(\sum_{k=1}^{n} c_k\right)}, \tag{A7}$$

$$\Gamma_S = \frac{\sum_{k=1}^{n} c_k\left(\frac{\bar{M}_k}{\bar{\bar{M}}}\right)^2 f_k^1 f_k^2 \varepsilon\left(\frac{r_k^1 - r_k^2}{\bar{r}_k}\right)^2}{\left(\sum_{k=1}^{n} c_k\right)}, \tag{A8}$$

where Ω, h, ν, θ_D, κ_L^{pure}, κ_L^{cal} and Γ are the average volume/atom, the Planck constant, the average sound velocity, the Debye temperature, the lattice thermal conductivity of the pure materials, the calculated lattice thermal conductivity of defected materials and the disorder scattering parameter, respectively.

Acknowledgments

This work was financially supported by the National Key Research and Development Program of China (Grant No. 2018YFA0702100), the Joint Funds of the National Natural Science Foundation of China and the Chinese Academy of Sciences' Large-Scale Scientific Facility (Grant No. U1932106), and the Sichuan University Innovation Research Program of China (Grant No. 2020SCUNL112).

References

[1] Gingerich D B and Mauter M S 2015 *Sci. Technol.* **49** 8297
[2] Chen Z Y, Wang R F, Wang G Y, Zhou X Y, Wang Z S, Yin C, Hu Q, Zhou B Q, Tang J and Ang R 2018 *Chin. Phys. B* **27** 047202
[3] Pei Y Z, Shi X Y, LaLonde A, Wang H, Chen L D and Snyder G J 2011 *Nature* **473** 66
[4] Tan G J, Zhao L D and Kanatzidis M G 2016 *Chem. Rev.* **116** 12123
[5] Fu C G, Bai S Q, Liu Y T, Tang Y S, Chen L D, Zhao X B and Zhu T J 2015 *Nat. Commun.* **6** 8144
[6] Li J, Zhang X Y, Wang X, Bu Z L, Zheng L T, Zhou B Q, Xiong F, Chen Y and Pei Y Z 2018 *J. Am. Chem. Soc.* **140** 16190
[7] Luo Z Z, Hao S Q, Zhang XM, Hua X, Cai ST, Tan G J, Bailey T P, Ma R C, Uher C, Wolverton C, Dravid V P, Yan Q Y and Kanatzidis M G 2018 *Energy Environ. Sci.* **11** 3220
[8] Yang J W, Li G D, Zhu H T, Chen N, Lu T B, Gao J L, Guo L W, Xiang J S, Sun P J, Yao Y, Yang R G and Zhao H Z 2022 *Joule* **6** 193
[9] Zhang X Y, Li J, Wang X, Chen Z W, Mao J J, Chen Y and Pei Y Z 2018 *J. Am. Chem. Soc.* **140** 15883
[10] Hong M, Lyu W Y, Wang Y, Zou J and Chen Z G 2020 *J. Am. Chem. Soc.* **142** 2672
[11] Chen Z W, Ge B H, Li W, Lin S Q, Shen J W, Chang Y J, Hanus R, Snyder G J and Pei Y Z 2017 *Nat. Commun.* **8** 13828
[12] Xiao Y, Wu H J, Li W, Yin M J, Pei Y L, Zhang Y, Fu L W, Chen Y X, Pennycook S J, Huang L, He J Q and Zhao L D 2017 *J. Am. Chem. Soc.* **139** 18732
[13] Luo Y B, Hao S Q, Cai S T, Slade T J, Luo Z Z, Dravid V P, Wolverton C, Yan Q Y and Kanatzidis M G 2020 *J. Am. Chem. Soc.* **142** 15187

[14] Yao C J, ZhangH L and Zhang Q C 2019 *Polymers* **11** 107
[15] Zhang Y C, Zhang Q C and Chen G M 2020 *Carbon Energy* **2** 408
[16] Imasato K, Fu C G, Pan Y, Wood M, Kuo J J, Felser C and Snyder G J 2020 *Adv. Mater.* **32** 1908218
[17] Shi X M, Zhao T T, Zhang X Y, Sun C, Chen Z W, Lin S Q, Li W, Gu H and Pei Y Z 2019 *Adv. Mater.* **31** 1903387
[18] Luo T, Kuo J J, Griffith K J, Imasato K, Cojocaru-Miredin O, Wuttig M, Gault B, Yu Y and Snyder G J 2021 *Adv. Funct. Mater.* **31** 2100258
[19] Chang C, Wu M H, He D S, Pei Y L, Wu C F, Wu X F, Yu H L, Zhu F Y, Wang K D, Chen Y, Huang L, Li J F, He J Q and Zhao L D 2018 *Science* **360** 778
[20] Zhao L D, Tan G J, Hao S Q, He J Q., Pei Y L, Chi H, Wang H, Gong S K, Xu H B, Dravid V P, Uher C, Snyder G J, Wolverton C and Kanatzidis M G 2016 *Science* **351** 141
[21] Liu Y, Calcabrini M, Yu Y, Lee S, Chang C, David J, Ghosh T, Spadaro M C, Xie C Y, Cojocaru-Miredin O, Arbiol J and Ibanez M 2021 *ACS Nano* **16** 78
[22] Peng K L, Lu X, Zhan H, Hui S, Tang X D, Wang G W, Dai J Y, Uher C, Wang G Y and Zhou X Y 2016 *Energy Environ. Sci.* **9** 454
[23] Hu Q, Yin C, Zhang L L, Lei L, Wang Z S, Chen Z Y, Tang J and Ang R 2018 *Chin. Phys. B* **27** 017104
[24] Pei Y L and Liu Y 2012 *J. Alloys Compd.* **514** 40
[25] Ramakrishnan A, Raman S, Chen L C and Chen K H 2017 *J. Electron. Mater.* **47** 3091
[26] Yin C, Liu H T, Hu Q, Tang J, Pei Y Z and Ang R 2019 *ACS Appl. Mater. Interfaces* **11** 48079
[27] Wang X Y, Yao H H, Zhang Z W, Li X F, Chen C, Yin L, Hu K N, Yan Y R, Li Z, Yu B, Cao F, Liu X J, Lin X and Zhang Q 2021 *ACS Appl. Mater. Interfaces* **13** 18638
[28] Perdew J P, Burke K and Ernzerhof M 1996 *Phys. Rev. Lett.* **77** 3865
[29] Blochl P E 1994 *Phys. Rev. B* **50** 17953
[30] Blochl, P E, Jepsen O and Andersen O K 1994 *Phys. Rev. B* **49** 16223
[31] Ji G Q, Han C Z, Hu S L, Fu P F, Chen X, Guo J G, Tang J and Xiao Z W 2021 *J. Am. Chem. Soc.* **143** 10275
[32] Kresse G and Furthmuller J 1996 *Phys. Rev. B* **54** 11169
[33] Luo Y R 2007 *Comprehensive Handbook of Chemical Bond Energies* (CRC Press)
[34] Poater J, Duran M, Sola M and Silvi B 2005 *Chem. Rev.* **105** 3911
[35] Zhou B Q, Li S, Li W, Li J, Zhang X Y, Lin S Q, Chen Z W and Pei Y Z 2017 *ACS Appl. Mater. Interfaces* **9** 34033
[36] May A F, Toberer E S, Saramat A and Snyder G J 2009 *Phys. Rev. B* **80** 125205
[37] Toberer E S, Zevalkink A, Crisosto N and Snyder G J 2010 *Adv. Funct. Mater.* **20** 4375
[38] Callaway J and von Baeyer H C 1960 *Phys. Rev.* **120** 1149
[39] Dey T K and Chaudhuri K D 1976 *J. Low Temp. Phys.* **23** 419
[40] Yang J, Meisner G P and Chen L 2004 *Appl. Phys. Lett.* **85** 1140
[41] Zaitsev V, Tkalenko E and Nikitin E 1969 *Sov. Phys. Solid State* **11** 3000
[42] Abeles B 1963 *Phys. Rev.* **131** 1906
[43] Slack G A 1957 *Phys. Rev.* **105** 829